

North Alabama Lightning Mapping Array (LMA): VHF Source Retrieval Algorithm and Error Analyses

W. J. KOSHAK,* R. J. SOLAKIEWICZ,⁺ R. J. BLAKESLEE,* S. J. GOODMAN,* H. J. CHRISTIAN,* J. M. HALL,[#]
J. C. BAILEY,[@] E. P. KRIDER,& M. G. BATEMAN,** D. J. BOCCIPPIO,* D. M. MACH,⁺⁺ E. W. McCAUL,**
M. F. STEWART,⁺⁺ D. E. BUECHLER,⁺⁺ W. A. PETERSEN,⁺⁺ D. J. CECIL⁺⁺

**Earth Science Department, NASA Marshall Space Flight Center, Huntsville, Alabama*

⁺Chicago State University, Chicago, Illinois

[#]Computer Sciences Corporation, Huntsville, Alabama

[@]Raytheon ITSS, Huntsville, Alabama

&The University of Arizona, Tucson, Arizona

***Universities Space Research Association, Huntsville, Alabama*

⁺⁺University of Alabama in Huntsville, Huntsville, Alabama

(Manuscript received 15 July 2003, in final form 21 October 2003)

ABSTRACT

Two approaches are used to characterize how accurately the north Alabama Lightning Mapping Array (LMA) is able to locate lightning VHF sources in space and time. The first method uses a Monte Carlo computer simulation to estimate source retrieval errors. The simulation applies a VHF source retrieval algorithm that was recently developed at the NASA Marshall Space Flight Center (MSFC) and that is similar, but not identical to, the standard New Mexico Tech retrieval algorithm. The second method uses a purely theoretical technique (i.e., chi-squared Curvature Matrix Theory) to estimate retrieval errors. Both methods assume that the LMA system has an overall rms timing error of 50 ns, but all other possible errors (e.g., anomalous VHF noise sources) are neglected. The detailed spatial distributions of retrieval errors are provided. Even though the two methods are independent of one another, they nevertheless provide remarkably similar results. However, altitude error estimates derived from the two methods differ (the Monte Carlo result being taken as more accurate). Additionally, this study clarifies the mathematical retrieval process. In particular, the mathematical difference between the first-guess linear solution and the Marquardt-iterated solution is rigorously established thereby explaining why Marquardt iterations improve upon the linear solution.

1. Introduction

The north Alabama Lightning Mapping Array (LMA) is a multisensor network that measures the time of arrival (TOA) of VHF radio waves produced by lightning. Mathematical inversion of the TOA data allows one to reconstruct the lightning channel in three-dimensional space and in time. Operationally, the raw TOA data stream is first processed to define what sets of TOA values belong to *single* VHF lightning “point” sources. But since this processing is imperfect, some of the derived sets actually correspond to VHF noise (e.g., television broadcast interference, local corona events from nearby power lines and transformers), or to a mixture of noise and lightning. Mathematical inversion of these anomalous cases can lead to spurious and/or deceptive results.

Moreover, an accurate grouping of VHF sources into flashes is essential for making good estimates of cell flash rate, an important derivable from the LMA. Thunderstorm cells often develop in close proximity to one another along clusters or lines while at the same time producing very high flash rates. These storm systems also produce individual lightning discharges that can easily extend from one cell to the next. When the flash rate and areal flash density increases, it can become difficult (sometimes impossible) to determine to which flash a particular VHF source belongs. The grouping process is particularly difficult if the VHF source retrieval error is large or unknown. Consequently, there is great interest in determining and understanding the specific characteristics of source retrieval errors across the LMA detection domain. One such community having this interest is the National Space Science and Technology Center’s (NSSTCs) Short-term Prediction Research and Transition (SPoRT) center. The SPoRT center seeks to accelerate the infusion of National Aeronautics and Space Administration (NASA) Earth Science En-

Corresponding author address: Dr. William J. Koshak, Earth Science Department, NASA Marshall Space Flight Center (MSFC), Huntsville, AL 35812.
E-mail: william.koshak@nasa.gov

terprise (ESE) observations, data assimilation (including LMA data) and modeling research into National Weather Service (NWS) forecast operations and decision-making at the regional and local level.

In this paper, an algorithm for retrieving the location and time-of-occurrence of VHF lightning sources from LMA TOA data is introduced, and the ability of the LMA to accurately retrieve single VHF lightning sources is examined and characterized in detail. Sensor timing error (50 ns) is accounted for, but all other forms of data contamination and processing imperfections are not considered. Section 2 describes the retrieval algorithm, and section 3 discusses two methods for estimating the retrieval errors. Section 4 provides error results, and section 5 provides conclusions.

2. VHF source retrieval algorithm

A VHF source retrieval algorithm has been developed at New Mexico Tech (NMT). It is a research-grade software product that is used in conjunction with a variety of LMA networks across the United States (P. Krehbiel and J. Harlin 2002, personal communication). For convenience/clarity, we developed an independent retrieval algorithm “from scratch” that is similar, but not identical to, the NMT algorithm. The new algorithm was written in the IDL programming language at the NASA-affiliated Global Hydrology and Climate Center (GHCC), and is hereafter called the “GHCC algorithm.” Having an intimate knowledge of all aspects of this algorithm has allowed us to fully assess algorithm test results. One should note that routine operational analyses of north Alabama LMA data are still, and have always been, performed using the NMT algorithm.

a. Overview

The GHCC algorithm retrieves VHF source location and time-of-occurrence, (x, y, z, t) , from LMA arrival time data. Atmospheric refraction is neglected (i.e., straight path wave propagation from source to LMA receiver is assumed). The algorithm involves a linear matrix inversion to obtain an initial solution estimate in Cartesian coordinates. This solution is improved using a simple altitude constraint followed by a standard iterative approach due to Marquardt (1963). The spatial portion of the final Marquardt-iterated solution (x_s, y_s, z_s, t_s) is mapped to 1984 World Geodetic System (WGS84) earth ellipsoid coordinates: $(\lambda = \text{longitude}, \phi = \text{geodetic latitude}, \zeta = \text{altitude})$. The WGS84 earth ellipsoid is actually a degenerate ellipsoid (i.e., an oblate spheroid) having equatorial radius (semimajor axis) equal to $6.378137 \times 10^6 \text{ m} \pm 2 \text{ m}$, and polar axis (semiminor axis) equal to $6.3567523142 \times 10^6 \text{ m}$ [see DMA (1991) for further details]. Hence, the oblate nature of the earth is accounted for in this work. The altitude ζ is an extremely close approximation to the true altitude above the WGS84 earth surface, and has

the advantage that it is far easier to code and compute (see appendix A).

b. Linear inversion of transit equation

A linear inversion can be performed to obtain the VHF source location and time of occurrence. It does not matter what fixed Cartesian coordinate system one uses to describe the problem, the *form* of the linear retrieval will remain unchanged. To emphasize this fact, we shall proceed by introducing a general Cartesian coordinate system (X, Y, Z) whose origin and orientation are arbitrary with respect to the earth. We define t to be the time of occurrence of the lightning VHF point source at location (X, Y, Z) , and the i th LMA sensor is located at (X_i, Y_i, Z_i) . The arrival time t_i of the VHF wave at the i th LMA sensor is given by the simple straight-path transit equation as provided in (1) of Koshak and Solakiewicz (1996):

$$t_i = t + \frac{1}{c}[(X_i - X)^2 + (Y_i - Y)^2 + (Z_i - Z)^2]^{1/2}, \quad (1)$$

where c is the speed of light in a vacuum (the index of refraction in the atmosphere is taken as unity). Rearranging gives

$$(X_i^2 + Y_i^2 + Z_i^2) - 2X_iX - 2Y_iY - 2Z_iZ + (X^2 + Y^2 + Z^2) = c^2(t_i^2 - 2t_it + t^2). \quad (2)$$

The terms nonlinear in (X, Y, Z, t) can be removed by simply picking the convention that $t_i \equiv 0$; that is, by defining the excitation time of LMA site 1 to be “0 s.” With this convention, (2) becomes (for $i = 1$)

$$c^2t^2 - X^2 - Y^2 - Z^2 = X_1^2 + Y_1^2 + Z_1^2 - 2X_1X - 2Y_1Y - 2Z_1Z. \quad (3)$$

Substituting (3) back into (2) for $i = 2, \dots, n$ gives the desired linear system

$$\begin{bmatrix} \frac{1}{2}(L_2^2 - c^2t_2^2 - L_1^2) \\ \vdots \\ \frac{1}{2}(L_n^2 - c^2t_n^2 - L_1^2) \end{bmatrix} = \begin{bmatrix} (X_2 - X_1) & (Y_2 - Y_1) & (Z_2 - Z_1) & -ct_2 \\ \vdots & \vdots & \vdots & \vdots \\ (X_n - X_1) & (Y_n - Y_1) & (Z_n - Z_1) & -ct_n \end{bmatrix} \begin{bmatrix} X \\ Y \\ Z \\ ct \end{bmatrix}, \quad (4)$$

where $L_i^2 = X_i^2 + Y_i^2 + Z_i^2$, and the LMA network is assumed to have $n \geq 5$ sensors. The linear system in (4) can be written in matrix-vector form as

$$\mathbf{g} = \mathbf{K}\mathbf{f}, \quad (5)$$

with linear least squares solution given as

$$\mathbf{f} = \begin{bmatrix} X \\ Y \\ Z \\ ct \end{bmatrix} = (\mathbf{K}^T \mathbf{K})^{-1} \mathbf{K}^T \mathbf{g}. \quad (6)$$

Here, T represents matrix transposition.

c. Specific coordinate systems

As discussed above, the solution in (6) will work for any fixed Cartesian coordinate system. In this section, we specify two such systems as shown in Fig. 1. In one case, a Cartesian coordinate system (u, v, w) can be used that has an origin at the center of the earth. The location of the VHF source is at

$$\mathbf{s} = u\hat{\mathbf{u}} + v\hat{\mathbf{v}} + w\hat{\mathbf{w}}, \quad (7)$$

where $u = s \cos\varphi \cos\lambda$, $v = s \cos\varphi \sin\lambda$, $w = s \sin\varphi$. Here, φ is spherical latitude and λ is longitude. Similar expressions can be obtained to describe the location \mathbf{s}_i of the i^{th} LMA sensor by simply subscripting all the variables ($\mathbf{s}, u, v, w, s, \varphi, \lambda$) with an “ i .” The altitude of the VHF source above the WGS84 surface is very well approximated by (see appendix A)

$$\zeta(\varphi) = s - \rho(\varphi), \quad (8)$$

where $\rho(\varphi) = [(\cos^2\varphi)/a^2 + (\sin^2\varphi)/b^2]^{-1/2}$ is the earth radius, and a and b are the semimajor (equatorial) and minor (polar) axes, respectively. The (u, v, w) Cartesian coordinate system is, in turn, related to a spherical coordinate system (s, φ, λ), where s is the distance from the center of the earth to the VHF source.

The VHF source location shown in Fig. 1 can also be defined with respect to a Cartesian coordinate system (x, y, z) whose origin is fixed at an arbitrary LMA site, say LMA site 1. The positive x direction ($\hat{\mathbf{x}}$) points eastward, the positive y direction ($\hat{\mathbf{y}}$) points approximately northward, and the positive z direction ($\hat{\mathbf{z}} = \hat{\mathbf{s}}_1$) points approximately toward the local zenith. If the earth was a perfect sphere, then $\hat{\mathbf{y}}$ and $\hat{\mathbf{z}}$ would point exactly north and toward the zenith, respectively. The VHF source location in this system is simply

$$\mathbf{r} = x\hat{\mathbf{x}} + y\hat{\mathbf{y}} + z\hat{\mathbf{z}}. \quad (9)$$

The two Cartesian coordinate systems $\{(u, v, w), (x, y, z)\}$ are related as follows:

$$\mathbf{s} = \mathbf{s}_1 + \mathbf{r} = \mathbf{s}_1 + \mathbf{A} \cdot \mathbf{p}, \quad (10)$$

where the vector $\mathbf{p} = x\hat{\mathbf{u}} + y\hat{\mathbf{v}} + z\hat{\mathbf{w}}$, and the dyadic \mathbf{A} is given by

$$\begin{aligned} \mathbf{A} = & -\sin\lambda_1\hat{\mathbf{u}}\hat{\mathbf{u}} - \sin\varphi_1\cos\lambda_1\hat{\mathbf{u}}\hat{\mathbf{v}} + \cos\varphi_1\cos\lambda_1\hat{\mathbf{u}}\hat{\mathbf{w}} \\ & + \cos\lambda_1\hat{\mathbf{v}}\hat{\mathbf{u}} - \sin\varphi_1\sin\lambda_1\hat{\mathbf{v}}\hat{\mathbf{v}} + \cos\varphi_1\sin\lambda_1\hat{\mathbf{v}}\hat{\mathbf{w}} \\ & + 0\hat{\mathbf{w}}\hat{\mathbf{u}} + \cos\varphi_1\hat{\mathbf{w}}\hat{\mathbf{v}} + \sin\varphi_1\hat{\mathbf{w}}\hat{\mathbf{w}}. \end{aligned} \quad (11)$$

Although the vector \mathbf{p} has components (x, y, z), it does *not* represent the vector $x\hat{\mathbf{x}} + y\hat{\mathbf{y}} + z\hat{\mathbf{z}}$. The explicit use of the coordinate unit vectors ($\hat{\mathbf{u}}, \hat{\mathbf{v}}, \hat{\mathbf{w}}$) in (11) reminds us of this fact. Carrying out the dot product on the right-hand side of (10) gives the explicit transformation equations between the two Cartesian coordinate systems

$$\begin{aligned} u &= u_1 - x \sin\lambda_1 - y \sin\varphi_1 \cos\lambda_1 + z \cos\varphi_1 \cos\lambda_1, \\ v &= v_1 + x \cos\lambda_1 - y \sin\varphi_1 \sin\lambda_1 + z \cos\varphi_1 \sin\lambda_1, \\ w &= w_1 + y \cos\varphi_1 + z \sin\varphi_1. \end{aligned} \quad (12)$$

d. Specific linear solutions

The general solution in (6) can be used to obtain solutions in the two Cartesian coordinate systems described in the previous section. Collectively, ($\mathbf{f}, \mathbf{g}, \mathbf{K}$) in (6) depend on the variables: ($X, Y, Z, t, X_i, Y_i, Z_i, t_i$); $i = 1, \dots, n$. To obtain the solution in the (u, v, w) system, the following substitutions ($X \rightarrow u, Y \rightarrow v, Z \rightarrow w, X_i \rightarrow u_i, Y_i \rightarrow v_i, Z_i \rightarrow w_i$) in (6) are made. Hence, the solution vector in this case is $\mathbf{f} = (u, v, w, ct) = (\mathbf{s}, ct)$ from which we extract the WGS84-based solution

$$\begin{aligned} \lambda &= \tan^{-1}\left(\frac{v}{u}\right), \quad \phi = \tan^{-1}\left(\frac{a^2}{b^2} \tan\varphi\right), \\ \zeta &= (u^2 + v^2 + w^2)^{1/2} - \rho(\varphi), \end{aligned} \quad (13)$$

where the spherical latitude $\varphi = \tan^{-1}(w/\sqrt{u^2 + v^2})$.

Similarly, to obtain the solution in the (x, y, z) system, we make the replacements ($X \rightarrow x, Y \rightarrow y, Z \rightarrow z, X_i \rightarrow x_i, Y_i \rightarrow y_i, Z_i \rightarrow z_i$) in (6). The solution vector in this case is $\mathbf{f} = (x, y, z, ct) = (\mathbf{r}, ct)$; a detailed interpretation of this solution is provided in appendix B. The retrieved values (x, y, z) can be substituted into (12) to obtain (u, v, w), which can in turn be substituted into (13) to obtain (λ, ϕ, ζ).

The linear solutions described above are quite good in horizontal position and time of occurrence, but have pronounced errors in altitude (see Figs. 3 and 5 later in the text, and the comments in section 4c, for specifics). *The fundamental reason for this is traceable to the fact that the altitude difference between the various LMA sensors is not very large.* For this reason, the linear solution is regarded only as a first guess, the final solution being derived from some improvement on this first guess.

e. Altitude constraints

The GHCC algorithm generates the linear Cartesian solution $\mathbf{f} = (\mathbf{r}, ct)$. We then apply a simple altitude constraint: if the retrieved altitude (third component of \mathbf{f}) is less than 0 km or greater than 20 km, it is reassigned to 8 km. [As discussed in section 2f, an iterative Marquardt technique is then applied to further improve \mathbf{f} .

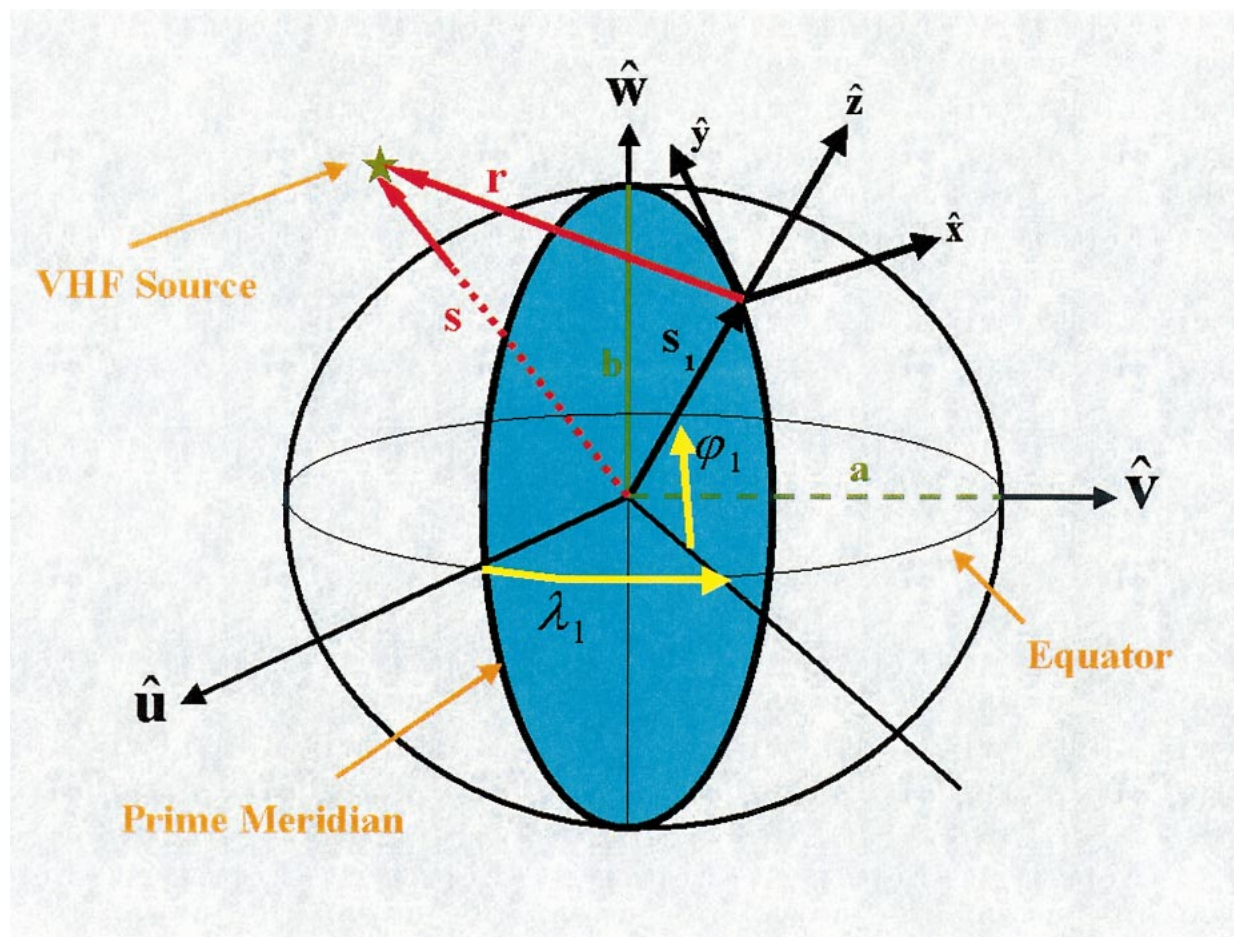


FIG. 1. Two Cartesian coordinate systems that can be used to describe VHF source location. The (u, v, w) Cartesian system origin is at the center of the earth and uses the s vector shown; this system is associated with a spherical coordinate system (s, φ, λ) . The (x, y, z) Cartesian system origin is at s_1 (the location of LMA site 1) and uses the r vector shown. Earth oblateness is a passive element of the geometry, but oblateness is accounted for when source altitude and sensor latitude are considered.

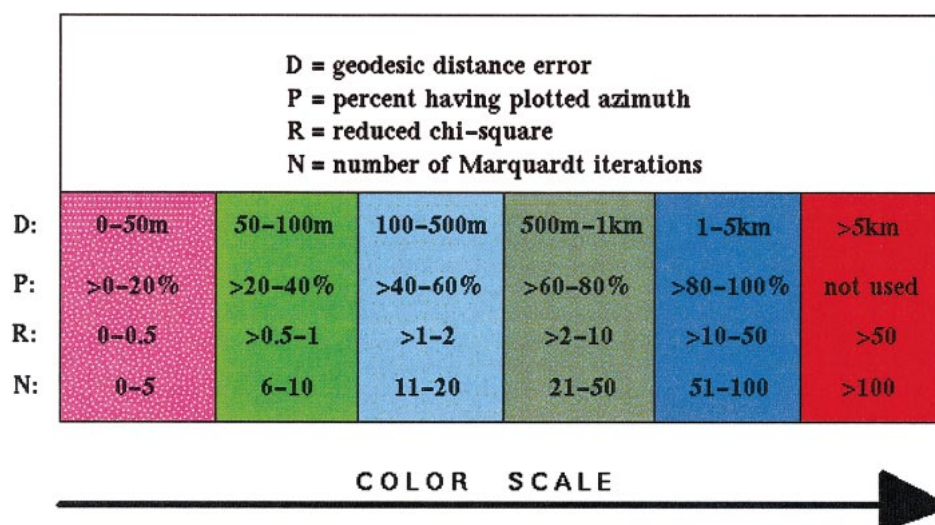


FIG. 2. Color scale for the plots that follow. The D -error scale is also used for plots of the following errors: $(x_{rms}, y_{rms}, z_{rms}, \zeta_{rms}, ct_{rms})$.

This combination of approaches produces considerably accurate solutions over a wide spatial domain (see section 4).]

Although it is beyond the scope of the current writing, one should note that it is possible to further improve solution accuracy by invoking more sophisticated means of improving the linear retrieval \mathbf{f} [see, e.g., the constrained linear inversion techniques discussed in Twomey (1977, chapter 6)]. Such an improvement can lead to quicker and more accurate solution convergence in the Marquardt algorithm. Because experimentation with such altitude constraints might be of interest in future studies, the GHCC algorithm purposely employs the

solution process $\mathbf{f} = (\mathbf{r}, ct) = (x, y, z, ct)$ rather than $\mathbf{f} = (\mathbf{s}, ct) = (u, v, w, ct)$ because it is easier to apply an altitude constraint to z rather than the more complicated term $w = s \sin \varphi$.

f. Marquardt iterations

In the GHCC algorithm, the altitude-constrained linear solution is improved using Marquardt iterations (see Marquardt 1963; Bevington 1969, chapter 11). Briefly, the Marquardt algorithm combines the best features of a gradient search with a Newton-type iteration. Noting that $\mathbf{f} = (\mathbf{r}, ct)$, one begins with a chi-squared goodness-of-fit function of the form

$$\begin{aligned}\chi^2(\mathbf{f}) &= \frac{1}{\sigma^2} \sum_{i=1}^n [M_i(\mathbf{f}) - ct_i]^2 \\ &= \frac{1}{\sigma^2} \sum_{i=1}^n \left[c \left\{ t + \frac{1}{c} [(x_i - x)^2 + (y_i - y)^2 + (z_i - z)^2]^{1/2} \right\} - ct_i \right]^2 \\ &= \frac{1}{\sigma^2} \sum_{i=1}^n \{ f_4 + [(x_i - f_1)^2 + (y_i - f_2)^2 + (z_i - f_3)^2]^{1/2} - ct_i \}^2,\end{aligned}\quad (14)$$

where $\sigma = c(50 \text{ ns}) = 15 \text{ m}$ is the rms distance-equivalent LMA sensor timing error. The model fitting function $M_i(\mathbf{f})$ is expanded in a Taylor series. The resulting χ^2 is then considered a function of the parameter increments $\Delta\mathbf{f} = (\Delta f_1, \Delta f_2, \Delta f_3, \Delta f_4)$, but all terms that are nonlinear in these increments are neglected. Taking a derivative of χ^2 with respect to the k th increment Δf_k and setting equal to zero results in a linear equation. Since $k = 1, \dots, 4$ there are four such linear equations. The linear system is solved for $\Delta\mathbf{f}$ so that the solution can be upgraded in the sense $\mathbf{f}' = \mathbf{f} + \Delta\mathbf{f}$. Diagonal terms are added to the matrix of the linear system to optimize convergence to the minimum. For example, the algorithm normally attempts Newton-type iterations. However, if it fails to reduce the χ^2 at any step, a parameter that weights the diagonal terms is modified so that the algorithm behaves more like a gradient search. The algorithm immediately attempts to return to a Newton-iteration as soon as it can. Marquardt iterations are terminated whenever the tolerance parameter $\tau = \text{norm}(\Delta\mathbf{f})/[\text{norm}(\mathbf{f}) + 0.001]$ is driven below 10^{-6} ; see Marquardt (1963) for additional details.

3. Methods for characterizing errors

a. Monte Carlo simulation

A $7^\circ \times 7^\circ$ region centered on the centroid of the LMA network was analyzed. The region was equally partitioned into subregions centered 0.05° apart so that 19 881 ($=141 \times 141$) source locations could be tested;

the source altitude is taken as constant across the analysis region. At the center of each subregion, 100 sources were analyzed. The analysis of each source was carried out as follows:

- 1) generate arrival times at each LMA sensor due to the source,
- 2) add timing error to each arrival time (to simulate actual arrival time data),
- 3) apply the GHCC algorithm to the simulated data to retrieve the source,
- 4) compute the retrieval error between the known source and retrieved source.

In step 2 above, the error added to each arrival time is chosen from a normal distribution having a mean of zero, and a standard deviation of 50 ns. In step 4, the mean geodesic distance error D along the WGS84 surface between the known and retrieved sources is computed, as well as the root-mean-square (rms) retrieval errors in the variables: x, y, z, ct, ζ . The azimuth A (0° – 360°) of the retrieved source relative to the known source is also computed. With three different VHF source altitudes ($z = 2, 7$, and 12 km), a total of 5 964 300 ($= 3 \times 19\,881 \times 100$) sources were analyzed in the Monte Carlo simulation. We also perform two additional simulations for VHF sources at $z = 7 \text{ km}$ that illustrate the effect of sensor altitudes and the effect of the simple altitude constraint and Marquardt iterations

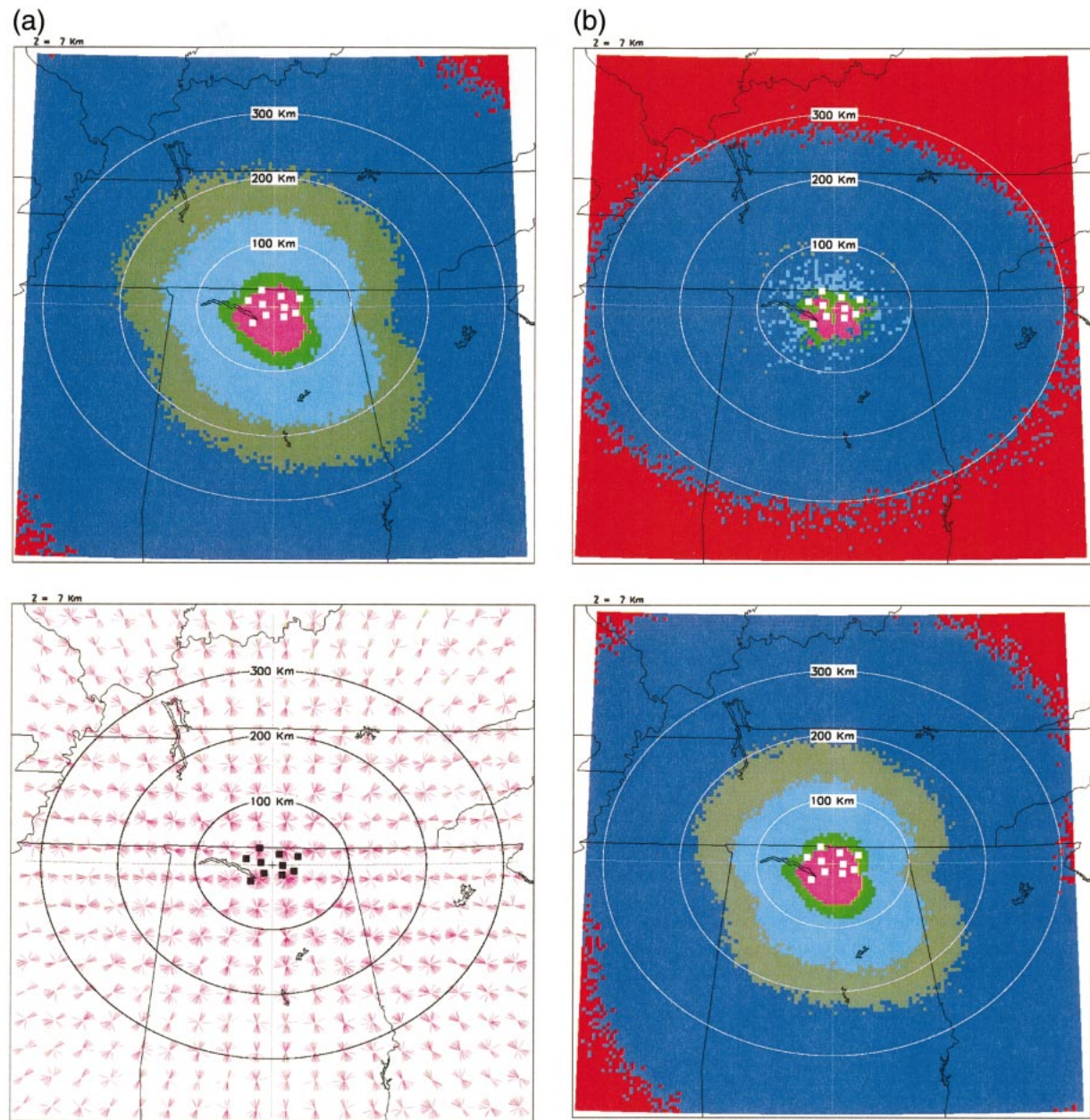


FIG. 3a. (top) Spatial distribution of the mean geodesic distance error D , and (bottom) azimuths A of retrieved sources relative to known source. Known sources are at $z = 7$ -km altitude, as indicated in the upper-left portion of each plot. See text for further description of the azimuth plot. Fig. 3b. (top) Spatial distribution of altitude error ζ_{rms} , and (bottom) the distance-equivalent timing error ct_{rms} . These error plots use the color scale in Fig. 2.

(see section 4 below for further details). Hence, a grand total of 9 940 500 ($= 5\,964\,300 + 2 \times 19\,881 \times 100$), or almost 10 million known sources have been simulated in this work.

Note that in our simulations we do not attempt to account for VHF noise sources. In addition, we assume that all sites in the network participate in the retrieval process. In actual LMA storm analyses, these two assumptions are often invalid. Nonetheless, our simula-

tions indicate what is realistically achievable by the LMA network.

b. Curvature Matrix Theory

As discussed in section 2f, the Marquardt algorithm is used to minimize a χ^2 function. The form of the χ^2 function was given in (14). As described in Bevington (1969; chapter 11), the diagonal elements of the inverse

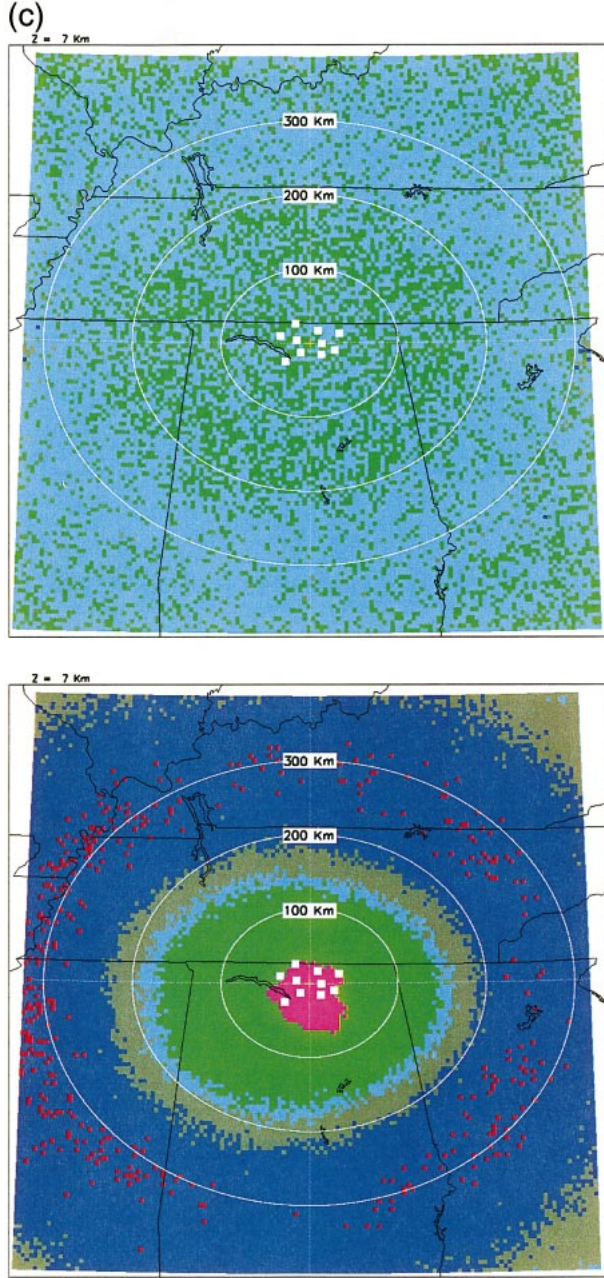


FIG. 3c. (top) Spatial distribution of the mean value of reduced chi-squared R , and (bottom) the mean value of the number of Marquardt iterations N required to converge to a solution.

of a curvature matrix \mathbf{C} can be used to estimate retrieval errors

$$C_{ij} = \frac{1}{2} \frac{\partial^2 \chi^2}{\partial f_i \partial f_j}; \quad \mathbf{E} = \mathbf{C}^{-1}; \quad \sigma_{f_j}^2 = E_{jj}. \quad (15)$$

Here, C_{ij} are the elements of the curvature matrix, and \mathbf{E} is an error matrix that is equal to the inverse of \mathbf{C} . Taking the square root of each diagonal element of \mathbf{E}

gives the desired error estimates: ($\sigma_{f_1} = \sigma_x$, $\sigma_{f_2} = \sigma_y$, ...) in the four unknowns (x , y , z , t).

4. Error results

A variety of error plots are provided in this section. Figure 2 describes the color scale associated with these plots. Each color represents a numerical range of values for a particular variable (e.g., the pink color represents geodesic distance errors between 0 and 50 m, but it also, for example, represents solutions that had from 0 to 5 Marquardt iterations). The maximum horizontal range for the plan view plots was determined by analyzing the line-of-site of the highest altitude sensor (see appendix C).

a. Monte Carlo tests of the GHCC algorithm

Figure 3a shows the spatial distribution of Monte Carlo results for D (top plot), and the specific angular distribution of azimuths A of the retrieved sources relative to known sources (bottom plot). There are 10 sites in the network, which has dimensions of 66.7 km in the east–west, and 51.1 km in the north–south. Each location on the D map is color-coded in accordance with Fig. 2 to indicate how well a known source (situated 7 km above the map location) is retrieved in geodesic distance. Note from the D map that the LMA can locate VHF sources to within 50 m (on average) when the sources are within or just outside the network perimeter. For the A map, line segments (centered on 6° bins) are used to indicate the azimuths of the retrieved sources relative to the known source. For example, suppose 12 (of the 100 sources analyzed at a given location) fell in a due easterly bin (87° – 93°) relative to the location. In this case, a due east (90°) line segment would be drawn from the given location, and it would be given a pink color pursuant to Fig. 2, since $P = 12/100 = 12\%$. Most retrieved azimuths are “directional” in the sense that the retrieved source falls roughly along a radial line running through the known source and the network centroid. However, if the source is closer to or over the network, the azimuth distribution tends to “fan out” meaning many values of A are statistically possible.

Figure 3b shows the spatial distribution of rms altitude errors (top panel) and rms distance-equivalent timing errors (bottom panel). The rms altitude errors are within 50 m over a portion of the network, but increase to above 5 km for distant (i.e., >300 km) sources. Overall, the altitude errors are sufficiently small to conduct many useful types of scientific investigations. If it were not for the simple altitude constraint and Marquardt iterations, the altitude errors would be far worse (see section 4c to follow). The values of D provided in Fig. 3a are smaller than the rms altitude errors (Fig. 3b, top) but about the same as the rms distance-equivalent timing errors (Fig. 3b, bottom).

Figure 3c shows the spatial distribution of mean val-

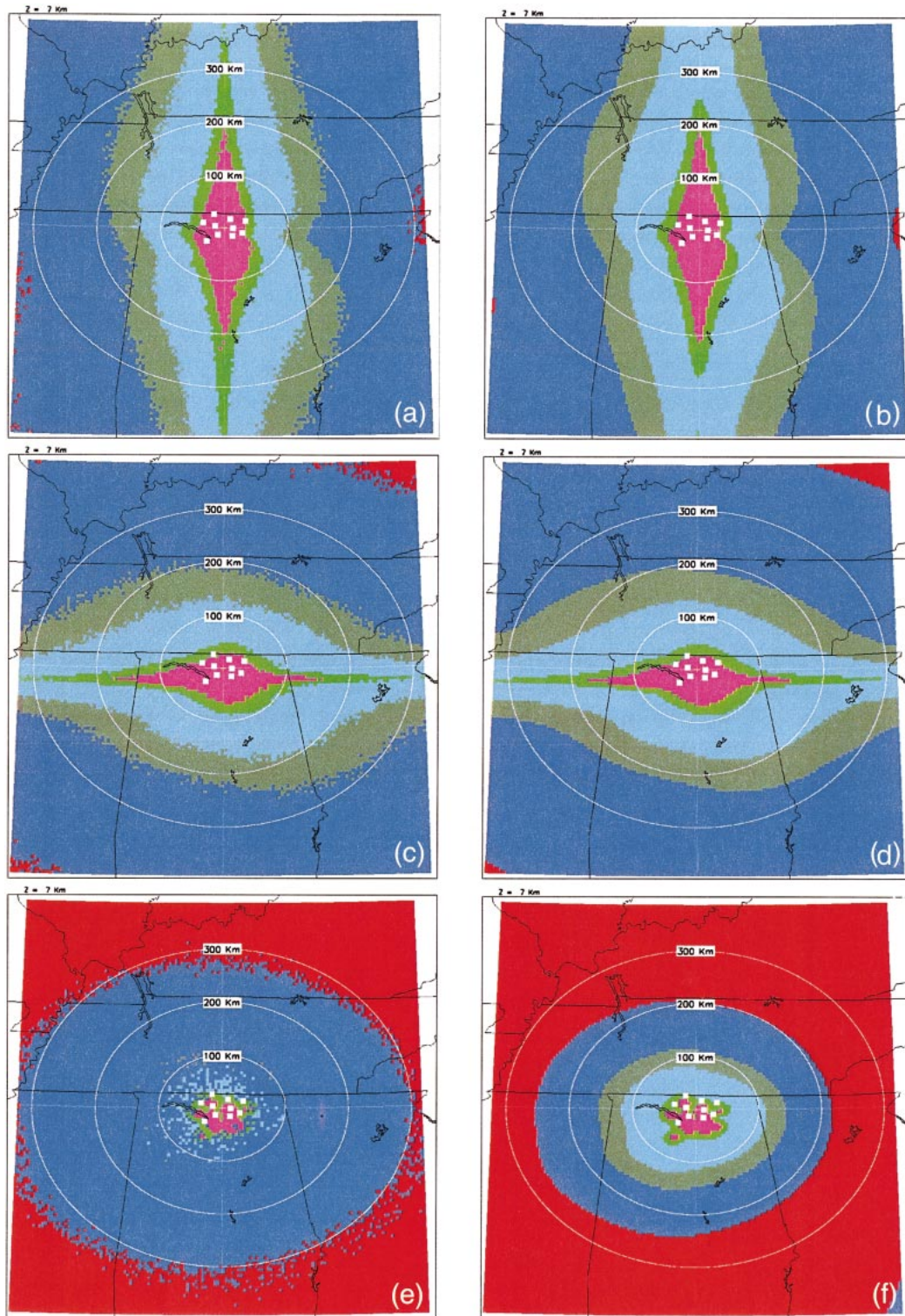


FIG. 4. Spatial distribution of Cartesian location errors: (top) x_{rms} , (middle) y_{rms} , and (bottom) z_{rms} derived from (left) Monte Carlo simulation and (right) the Curvature Matrix Theory. Spatial distribution of ct_{rms} (facing page) derived from (left) Monte Carlo simulation and (right) the Curvature Matrix Theory.

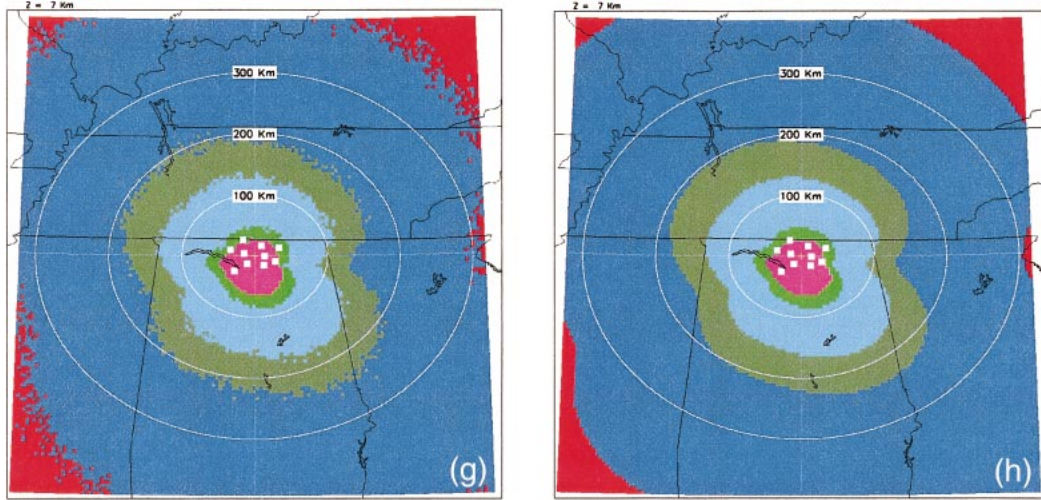


FIG. 4. (Continued)

ues of reduced chi-squared $R \equiv \chi^2/(n - \nu) = \chi^2/6$ (top) and the mean number of Marquardt iterations N required for a final solution (bottom). Here, n is the number of sensors in the LMA network (i.e., 10), and ν is the number of unknowns in the problem (i.e., the dimension of \mathbf{f} which is four).

According to the chi-squared statistical theory discussed in Bevington (1969, chapter 10), a value of $R = 1$ implies that the model-fitting function $M_i(\mathbf{f})$ is a good approximation to the parent function. A value of $R < 1$ implies the same, but does not indicate any improvement of the fit relative to the case $R = 1$. From Figs. 2 and 3c, we see that the mean of R is less than or equal to unity for many map locations. Interestingly, the bottom plot in Fig. 3c shows that there is a scattered “ring of fire” near a range of about 300 km. Here, solution convergence required more Marquardt iterations than elsewhere in the analysis region. Moreover, the number of Marquardt iterations required actually decreases in the four distant corners of the plot.

b. Comparing simulations with theory

It is natural to wonder how well the Monte Carlo and Curvature Matrix Theory error analyses agree in estimating LMA retrieval errors. The rms values ($x_{\text{rms}}, y_{\text{rms}}, z_{\text{rms}}, ct_{\text{rms}}$) from the Monte Carlo simulation are provided in the left-hand column of Fig. 4, and the associated error estimates from the Curvature Matrix Theory are provided in the right-hand column. To the best of our knowledge, this is the first time that detailed comparisons of this kind have been made. Since the Monte Carlo approach tests an actual TOA retrieval algorithm (namely the GHCC algorithm), it is considered to be the more rigorous error estimate. One can see from Fig. 4 that there is remarkably good agreement between the two (independent) error estimation approaches. One exception is in the estimation of z retrieval errors. For the

most part, and for the $z = 7$ km sources altitudes tested here, the Curvature Matrix Theory overestimates the altitude retrieval error. It occasionally underestimates altitude errors for some (x, y) source locations.

c. Effect of altitude constraint and Marquardt iterations

Recall that Fig. 3 provided error results for the GHCC algorithm for sources at $z = 7$ km. As discussed, the GHCC algorithm uses a simple altitude constraint and Marquardt iterations. To illustrate their importance, we deactivated them and reran the Monte Carlo analyses. In other words, we ran a Monte Carlo simulation on solutions derived solely from the linear inversion $\mathbf{f} = (\mathbf{r}, ct)$ described in section 2d; as always, this linear solution was mapped back to (λ, ϕ, ζ) coordinates. We found that the linear solution produced errors (D, ct_{rms}) that were very similar to, but slightly larger than, the (D, ct_{rms}) errors provided in Fig. 3. However, the errors ζ_{rms} (see Fig. 5) were substantially larger than the ζ_{rms} errors shown in Fig. 3. Hence, the altitude constraint together with Marquardt iterations help to substantially reduce altitude retrieval errors. Indeed, errors over the network are reduced from (at least) 1 km to below 50 m, or an improvement of at least a factor of 20. A detailed mathematical reason as to why the Marquardt algorithm improves the altitude retrieval is provided in appendix B. In short, the Marquardt algorithm improves altitude retrievals because it minimizes a different (and more appropriate) error function than does the linear retrieval.

d. Effect of sensor altitude

One might wonder why the linear retrieval $\mathbf{f} = (\mathbf{r}, ct)$ leads to large altitude retrieval errors z_{rms} [or ζ_{rms}]. It turns out that the large errors arise from insufficient

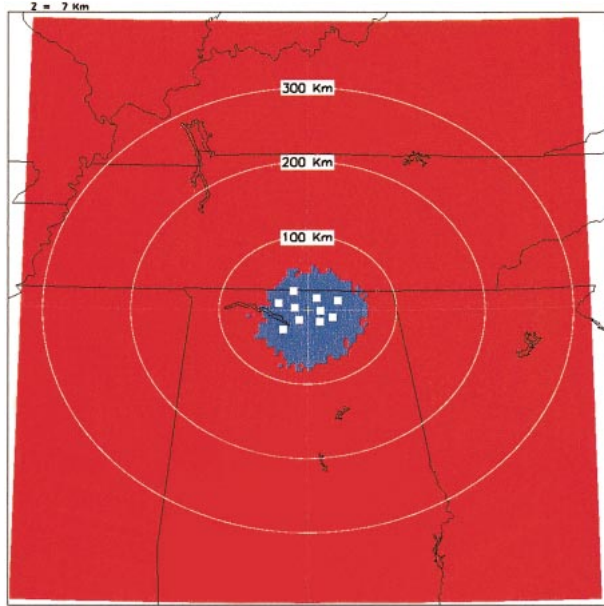


FIG. 5. Spatial distribution of ζ_{rms} when the altitude constraint and Marquardt routine are deactivated within the GHCC algorithm. Note that the altitude errors are larger here than in the top plot of Fig. 3b, which shows results with the altitude constraint and Marquardt routine activated.

vertical separation among the sensors within the LMA network. This is a geometrical effect as illustrated in Fig. 6; the red star indicates the location of a VHF source, and the solid black squares represent the sensors. For the i th sensor, (1) gives

$$(x_i - x)^2 + (y_i - y)^2 + (z_i - z)^2 = B_i^+,$$

$$(x_i - x)^2 + (y_i - y)^2 + (z_i - z)^2 = B_i^-, \quad (16)$$

where $B_i^\pm = c^2(t_i \pm 50 \text{ ns} - t)^2$ are constants. The two equations in (16) define two concentric spheres with origin at the i th sensor location $\mathbf{r}_i = (x_i, y_i, z_i)$. The inner sphere radius is B_i^- and the outer sphere radius is B_i^+ . If we consider just one sensor, the VHF source must be located somewhere on the inner or outer concentric

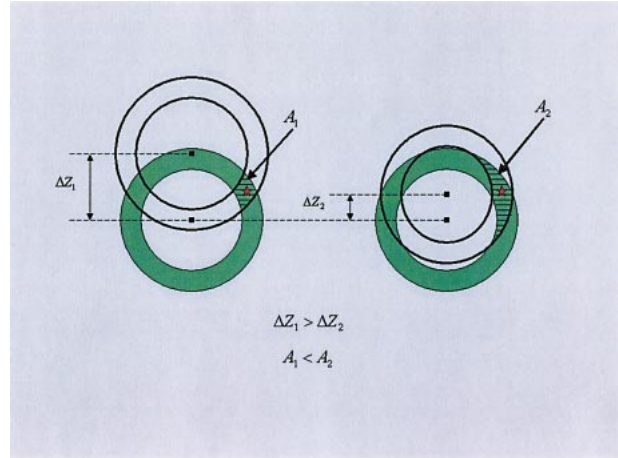


FIG. 6. Effect of sensor vertical separation on altitude retrieval error. When the upper sensor is moved closer to the lower sensor, the hatched area (denoting a portion of the projected solution uncertainty) increases. The location of the VHF source (denoted by the red star) stays fixed.

spherical surfaces, or within the volume bounded by these surfaces. We call this domain of possible VHF source locations the *spherical shell volume* V defined by one sensor. With two sensors, there are two spherical shell volumes (V_1, V_2) and the VHF source location is constrained to be within the volume defined by the intersection of these two volumes; that is, the volume $\Omega \equiv (V_1 \cap V_2)$. Figure 6 shows a simple example for

TABLE 1. Actual and virtual LMA sensor altitudes. The 10 sensors within the LMA network showing actual and fictitiously assigned sensor altitudes.

Site	Site name	Sensor altitudes in actual LMA network (km)	Sensor altitudes in virtual LMA network (km)
1	A&M	0.2186	0.1
2	Ardmore	0.2881	1.0
3	Boeing	0.1720	2.0
4	Fire tower	0.2397	0.5
5	Green Mountain	0.4652	5.0
6	Hospital	0.2137	10.0
7	Keel Mountain	0.4865	8.0
8	Monte Sano	0.5074	7.0
9	Owens	0.2299	9.0
10	Putman	0.5211	4.0

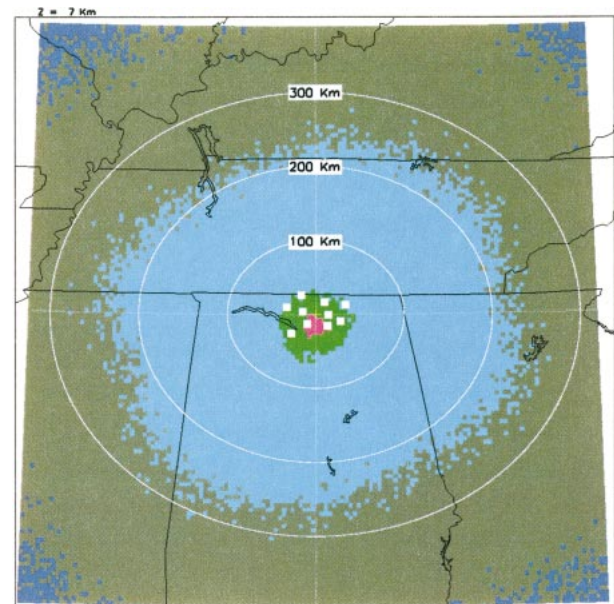


FIG. 7. Spatial distribution of ζ_{rms} for the virtual LMA network when the altitude constraint and Marquardt routine are deactivated within the GHCC algorithm. Note that these errors are far less than that shown in Fig. 5 for the actual network. The only difference between the virtual and actual networks is the sensor altitudes as shown in Table 1.

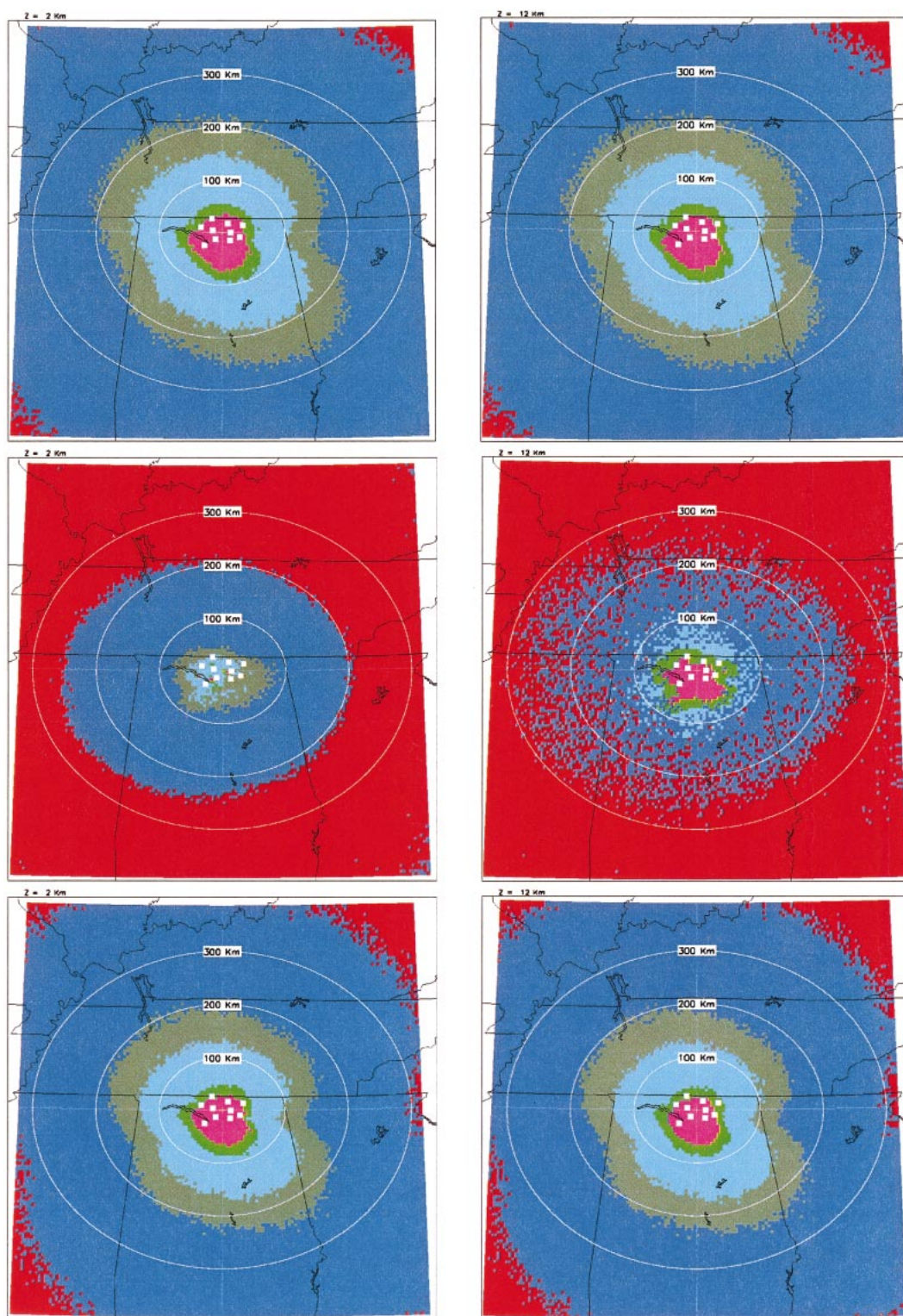


FIG. 8. Spatial distribution of (top) D , (middle) ζ_{rms} , and (bottom) $c\zeta_{\text{rms}}$ for known source altitudes of (left) $z = 2$ km and (right) $z = 12$ km.

two vertically separated sensors; the 3D geometry is projected into the vertical plane. A portion of the projected intersection of spherical shells is shown as a hatched area (left diagram in Fig. 6). Note that when the top sensor is moved closer to the bottom sensor (right diagram in Fig. 6), the fix on the VHF source location worsens (i.e., the hatched area increases).

To demonstrate and further clarify the specific nature of this geometrical effect, we again performed a Monte Carlo simulation on the linear algorithm $\mathbf{f} = (\mathbf{r}, ct)$; that is, on the GHCC algorithm with both the altitude constraint and Marquardt routine deactivated. However, this time we conducted the simulation on a different (i.e., virtual) sensor network. The virtual network is identical to the actual LMA network except that the virtual sensors span a much greater vertical range (see Table 1). Once again, we found that the errors (D, ct_{rms}) were very similar to the (D, ct_{rms}) errors provided in Fig. 3. However, the values of ζ_{rms} (see Fig. 7) were significantly smaller than that provided in Fig. 5. This specifically illustrates the geometrical effect depicted in Fig. 6.

e. Effect of source altitude

As a final test of the GHCC algorithm, we performed Monte Carlo simulations for known sources at $z = 2$ km, and $z = 12$ km, respectively. The results are provided in Fig. 8 and can be compared with the earlier results in Fig. 3 for $z = 7$ km. We found little difference in the (D, ct_{rms}) errors for $z = 2, 7$, and 12 km. However, there are some noteworthy differences in ζ_{rms} errors for the three source altitudes (i.e., compare the top plot of Fig. 3b with the middle plots of Fig. 8). The altitude retrieval is typically more accurate when the source is at $z = 7$ km than when at $z = 2$ or 12 km. In general, ζ_{rms} need not monotonically increase with range; such an assertion is an oversimplification. The magnitude of ζ_{rms} depends on source location, network geometry, specific simulated measurement errors, accuracy of first-guess location (from the linear inversion), and on the specific shape of the χ^2 hypersurface. For example, the presence of relative minima in χ^2 can have a dramatic impact on error results.

5. Conclusions

As we have stated, an accurate grouping of VHF sources into flashes is essential for estimating cell flash rate, an important derivable from the LMA. But if the VHF source retrieval error is large or unknown, the accuracy of such VHF source groupings and the computed flash rate is suspect.

The results provided in Fig. 3 (and other plots not shown for reasons of brevity) now quantify LMA re-

trieval errors across a large domain, and to exceptional spatial resolution. Consequently, these results will directly benefit and improve LMA-derived flash rate estimates. Overall, the error analyses provide insight to researchers who apply LMA data to a variety of studies (e.g., severe weather warning/forecasting, lightning satellite ground-validation, lightning physics, lightning climatology). For example, the azimuth plot in Fig. 3a (bottom) shows an interesting radial elongation (“spoking”) error that can be seen in real LMA storm analyses, but is herein quantified. Despite the advantages of this work, it is important to emphasize that the error results are “best case” scenarios since we have neglected VHF noise, and since we have assumed that all 10 sites participate in the retrieval process. In real LMA storm analyses this is seldom the case.

In addition, the results provided in this work are of mathematical significance. First, we have shown exactly why Marquardt iterations improve upon a linear inversion: the linear inversion minimizes one error function with a side constraint, whereas the Marquardt algorithm minimizes a closely related, but more appropriate, error function. Second, we have shown that two independent error analyses (a Monte Carlo simulation of actual inversions, and a theoretical approach based on Curvature Matrix Theory) provide remarkably similar results except for the altitude retrieval error. Because the Monte Carlo simulation employs (and tests) and actual TOA inversion algorithm (the GHCC algorithm), the Monte Carlo results are more realistic/accurate than the Curvature Matrix Theory results. Therefore, the Curvature Matrix Theory both underestimates and overestimates LMA altitude retrieval errors (depending on source location relative to the network). This statement is important since some retrieval error analyses of LMA networks across the United States have used the Curvature Matrix Theory.

Acknowledgments. This research was supported by the NASA Headquarters Validation Program, NRA 97-MTPE-03, under the direction of David O’C. Starr and by the NASA Earth Observing System program under Task 621-1598. We are grateful to the NSSTC’s SPoRT center for their support under Task 622-4102. In addition, we thank several New Mexico Tech researchers (Paul Krehbiel, Ron Thomas, William Rison, Timothy Hamlin, Jeremiah Harlin) for their guidance in helping us install the north Alabama LMA, and for their insightful discussions regarding data processing issues and error analyses. Thanks are also given to the NASA Faculty Fellowship Program for allowing us to bring coauthor Dr. Richard Solakiewicz to GHCC during summer 2002 to support these studies. We also thank Martin Murphy of Vaisala, Inc., for his useful comments regarding LMA error analyses. Finally, we are indebted to the NASA Marshall Space Flight Center Technology

Transfer Office for their assistance in procuring LMA hardware.

APPENDIX A

Approximating Source Altitude above the Oblate Earth

Recall that the GHCC algorithm produces a solution vector $\mathbf{f} = (x_s, y_s, z_s, ct_s)$. Using the transformations in (12) and (13), the spatial portion of this solution is converted to $(\lambda = \text{longitude}, \phi = \text{geodetic latitude}, \zeta = \text{altitude})$ coordinates. Figure A1 shows the geometry involved. Note that ζ is not quite the true altitude of the VHF source above the oblate earth surface. The true altitude of the VHF source is shown as the variable h . The numerical difference between ζ and h is negligible when ζ is small as is the case for all LMA VHF source retrievals. Figure A1 purposely places the VHF source at an unrealistically high altitude to clarify the geometrical/numerical difference between ζ and h .

The computation of ζ is straightforward. From (13) we had

$$\zeta(u, v, w) = (u^2 + v^2 + w^2)^{1/2} - \rho, \quad (\text{A1})$$

where $\rho = \rho(\varphi(u, v, w)) = [(\cos^2 \varphi)/a^2 + (\sin^2 \varphi)/b^2]^{-1/2}$ is the earth radius, and the spherical latitude $\varphi = \varphi(u, v, w) = \tan^{-1}(w/\sqrt{u^2 + v^2})$. The constants $a = 6.378137 \times 10^6$ m and $b = 6.3567523142 \times 10^6$ m

are the mean equatorial and polar radii of the Earth, respectively (DMA 1991). Note that (A1) is a highly simple/economical calculation given (u, v, w) .

Obtaining the correct height h takes some extra effort and, as we will see, gains us little. The elliptical curve defining the projected oblate earth surface in Fig. A1 can be described by

$$F(q, w) = \frac{q^2}{a^2} + \frac{w^2}{b^2} - 1 = 0, \quad (\text{A2})$$

where $q^2 = u^2 + v^2$. The gradient of F evaluated at a point G on the surface of the earth directly below the VHF source is a normal vector \mathbf{n} given by

$$\mathbf{n} = n\hat{\mathbf{n}} = \frac{1}{2}\nabla F|_G = \frac{q_G}{a^2}\hat{\mathbf{q}} + \frac{w_G}{b^2}\hat{\mathbf{w}}, \quad (\text{A3})$$

where (q_G, w_G) defines point G, and the factor of $1/2$ was inserted for convenience. Since the VHF source resides at location (q, w) , there exists some factor μ such that

$$q_G\hat{\mathbf{q}} + w_G\hat{\mathbf{w}} + \mu\mathbf{n} = q\hat{\mathbf{q}} + w\hat{\mathbf{w}}. \quad (\text{A4})$$

Substituting (A3) into (A4), simplifying, and equating components gives

$$q_G = \frac{q}{1 + \mu/a^2}, \quad w_G = \frac{w}{1 + \mu/b^2}. \quad (\text{A5})$$

Using (A5) to evaluate $F(q_G, w_G)$ yields a quartic equation in the factor μ given by

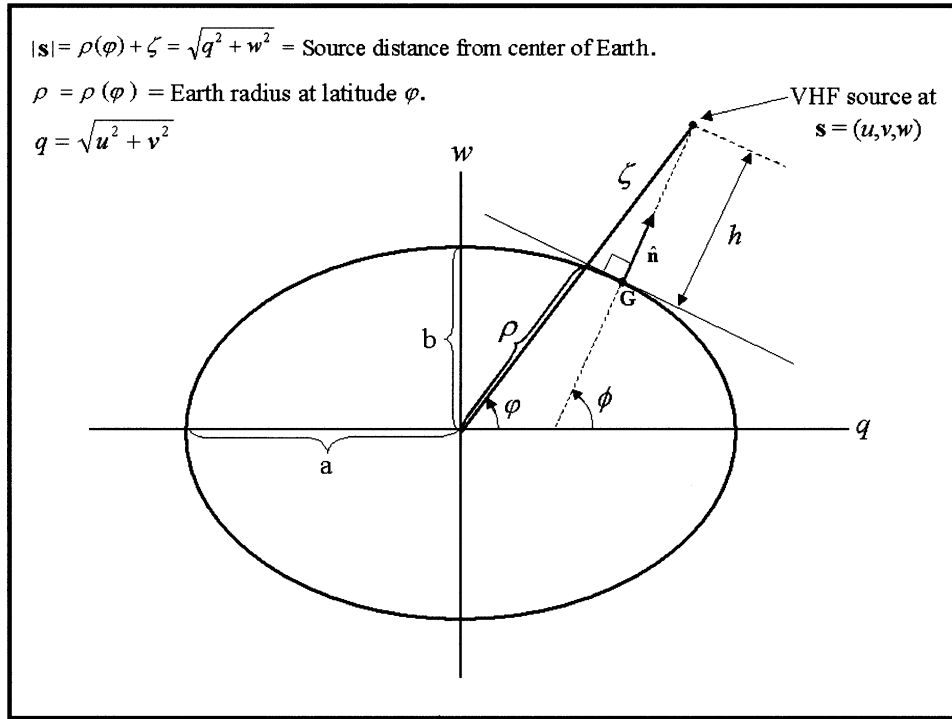


FIG. A1. True height h above the oblate earth surface, and altitude ζ as calculated in the GHCC algorithm. The numerical difference between h and ζ is exceedingly small (see Fig. A2). We have made ζ unrealistically large in this figure to clarify how it differs from h .

$$\mu^4 + 2(a^2 + b^2)\mu^3 + [(a^2 + b^2)^2 + 2a^2b^2 - a^2q^2 - b^2w^2]\mu^2 + 2a^2b^2(a^2 + b^2 - q^2 - w^2)\mu + a^2b^2(a^2b^2 - b^2q^2 - a^2w^2) = 0. \quad (\text{A6})$$

There are four roots to this equation (Beyer 1980); for brevity we omit the explicit, and rather lengthy, expressions for the roots. For VHF sources in the vicinity of the LMA where both $q < a$ and $w < b$ will hold, all coefficients in (A6) are positive except the last (constant term) coefficient. Hence, Descartes' "Law of Signs" (Barnett and Ziegler 1989, chapter 6) indicates that there will be only one positive real root among the four roots. Upon obtaining the appropriate root from (A6), (A5) can be used to obtain (q_G, w_G) . Noting that $q = \sqrt{u^2 + v^2}$, the calculation of the true height is then given by the familiar distance formula

$$h(u, v, w) = \sqrt{[(u^2 + v^2)^{1/2} - q_G]^2 + (w - w_G)^2}. \quad (\text{A7})$$

Hence, the error ε in using ζ to approximate h is obtained by differencing (A1) with (A7)

$$\varepsilon(u, v, w) = \zeta(u, v, w) - h(u, v, w). \quad (\text{A8})$$

Of course, this error increases for sources with the highest altitudes. Taking $\zeta = 20$ km (a very high altitude VHF source), and solving the quartic in (A6) so that h in (A7) can be computed, we found that the error ε is under 120 mm as shown in Fig. A2. Since this error is negligible, and since computing ζ is far simpler than computing h [which involves solving the quartic equation of (A6) each time a retrieval is performed], the GHCC algorithm implements the simple expression in (A1).

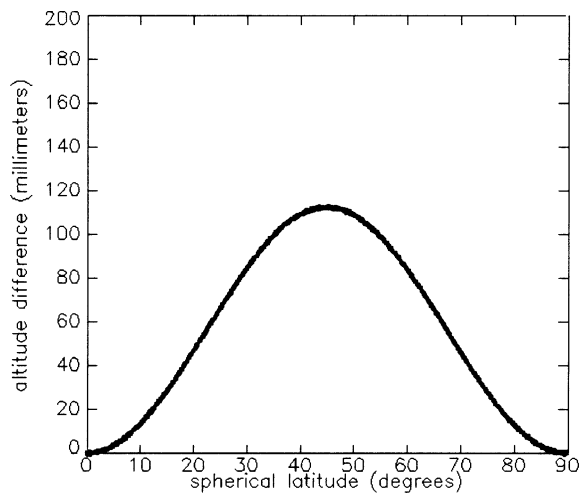


FIG. A2. The extremely small error ($\varepsilon = \zeta - h$) involved in estimating h with ζ . Here, $\zeta = 20$ km. For smaller values of ζ , the peak decreases.

APPENDIX B

Significance of the Linear Solution, $\mathbf{f} = (\mathbf{r}, ct)$

In this appendix we clarify the mathematical significance of the linear solution provided in section 2d of the main text, which can be summarized for $i = 1, \dots, n$ sensors as

$$\mathbf{f} = \begin{bmatrix} x \\ y \\ z \\ ct \end{bmatrix} = (\mathbf{K}^T \mathbf{K})^{-1} \mathbf{K}^T \mathbf{g},$$

$$\mathbf{K} = \begin{bmatrix} (x_2 - x_1) & (y_2 - y_1) & (z_2 - z_1) & -ct_2 \\ \vdots & \vdots & \vdots & \vdots \\ (x_n - x_1) & (y_n - y_1) & (z_n - z_1) & -ct_n \end{bmatrix},$$

$$\mathbf{g} = \begin{bmatrix} \frac{1}{2}(r_2^2 - c^2 t_2^2 - r_1^2) \\ \vdots \\ \frac{1}{2}(r_n^2 - c^2 t_n^2 - r_1^2) \end{bmatrix}, \quad r_i^2 = x_i^2 + y_i^2 + z_i^2. \quad (\text{B1})$$

To do this, we first generalize a constrained least squares linear retrieval result provided in Twomey (1977, chapter 6), and then demonstrate how the linear result in (B1) is a minimum of a particular error function.

Given a set of measurements \mathbf{y} , we are interested in finding an independent vector \mathbf{x} that minimizes the following error function

$$e(\mathbf{x}) = (\mathbf{y} - \mathbf{A}\mathbf{x})^2 + \gamma(\mathbf{x}^T \mathbf{H} \mathbf{x} + \mathbf{v}^T \mathbf{x} + \alpha). \quad (\text{B2})$$

Here, \mathbf{A} and \mathbf{H} are arbitrary real matrices, (\mathbf{v}^T, α) are constants, and γ is a constant that weights how strongly one wishes to emphasize the constraint term $(\mathbf{x}^T \mathbf{H} \mathbf{x} + \mathbf{v}^T \mathbf{x} + \alpha)$. [If one restricts \mathbf{H} to be symmetric, and specifies that $\mathbf{v}^T = \mathbf{0}$, $\alpha = 0$, then (B2) reduces to the same error function examined in Twomey (1977, section 6.3).] Assuming there are $i = 1, \dots, n$ measurements, and $j = 1, \dots, p$ unknowns, the expression in (B2) can be rewritten in component form as

$$e(\mathbf{x}) = \sum_{i=1}^n \left(y_i - \sum_{j=1}^p A_{ij} x_j \right)^2 + \gamma \left[x_1 \left(\sum_{j=1}^p x_j H_{j1} \right) + \dots + x_k \left(\sum_{j=1}^p x_j H_{jk} \right) + \dots + x_p \left(\sum_{j=1}^p x_j H_{jp} \right) + \sum_{j=1}^p v_j x_j + \alpha \right]. \quad (\text{B3})$$

Taking the derivative of (B3) and setting equal to zero

(i.e., $\partial e/\partial x_k = 0$; $k = 1, \dots, p$), and carrying out some algebra yields the linear system of equations

$$\sum_{j=1}^p \left[\sum_{i=1}^n A_{ik} A_{ij} + \frac{\gamma}{2} (H_{kj} + H_{jk}) \right] x_j + \frac{\gamma}{2} v_k = \sum_{i=1}^n A_{ik} y_i. \quad (\text{B4})$$

Since $k = 1, \dots, p$ (B4) can be written in matrix–vector notation as

$$\left[\mathbf{A}^T \mathbf{A} + \frac{\gamma}{2} (\mathbf{H} + \mathbf{H}^T) \right] \mathbf{x} + \frac{\gamma}{2} \mathbf{v} = \mathbf{A}^T \mathbf{y}. \quad (\text{B5})$$

So the value of \mathbf{x} that minimizes (B2) is

$$\mathbf{x} = \left[\mathbf{A}^T \mathbf{A} + \frac{\gamma}{2} (\mathbf{H} + \mathbf{H}^T) \right]^{-1} \left(\mathbf{A}^T \mathbf{y} - \frac{\gamma}{2} \mathbf{v} \right). \quad (\text{B6})$$

We identically recover the constrained linear inversion result $\mathbf{x} = (\mathbf{A}^T \mathbf{A} + \gamma \mathbf{H})^{-1} \mathbf{A}^T \mathbf{y}$ in Twomey [1977, Eq. (6.4)] as a special case of (B6) when \mathbf{H} is symmetric and ($\alpha = 0$, $\mathbf{v}^T = 0$); that is, \mathbf{H} symmetric $\Rightarrow (\gamma/2)(\mathbf{H} + \mathbf{H}^T) = (\gamma/2)(2\mathbf{H}) = \gamma \mathbf{H}$, and $\mathbf{v}^T = 0 \Rightarrow \mathbf{v} = 0$. The result in (B6) is of general use in a wide range of linear inversion problems that require the flexible application of physical constraints beyond those afforded by the measurements contained in \mathbf{y} . If no physical constraints are applied beyond the measurements \mathbf{y} (i.e., if $\gamma = 0$), then (B2) and (B6) reduce to the familiar least squares result; that is, the minimum of $(\mathbf{y} - \mathbf{A}\mathbf{x})^2$ is $\mathbf{x} = (\mathbf{A}^T \mathbf{A})^{-1} \mathbf{A}^T \mathbf{y}$.

Next, we clarify the significance of the linear retrieval in (B1). The fundamental TOA transit equation can be written

$$t_i = t + \frac{1}{c} |\mathbf{r}_i - \mathbf{r}|. \quad (\text{B7})$$

To solve (B7), we considered in (14) an error function of the form

$$E = \sigma^2 \chi^2 = \sum_{i=1}^n [|\mathbf{r}_i - \mathbf{r}| - c(t_i - t)]^2. \quad (\text{B8})$$

However, in order to understand the significance of the linear solution in (B1), we consider a closely related error function that is subject to a side constraint

$$\Psi(\mathbf{f}) = \frac{1}{2} \sum_{i=1}^n [|\mathbf{r}_i - \mathbf{r}|^2 - c^2(t_i - t)^2], \quad \text{side constraint: } t_1 \equiv 0. \quad (\text{B9})$$

Here, $\mathbf{f} = (\mathbf{r}, ct)$ and the factor $1/2$ has been inserted for convenience. Expanding the first equation in (B9) and noting that $r^2 = x^2 + y^2 + z^2$ we get

$$\begin{aligned} \Psi(\mathbf{f}) = \frac{1}{2} \sum_{i=1}^n \{ (r^2 - c^2 t^2) \\ - 2[x_i x + y_i y + z_i z - c t_i (ct)] \\ + (r_i^2 - c^2 t_i^2) \}. \end{aligned} \quad (\text{B10})$$

Applying the side constraint in (B9) to the transit equation in (B7) immediately gives $r^2 - c^2 t^2 = 2(x_1 x + y_1 y + z_1 z) - r_1^2$. This relation can be used to remove the nonlinear term $r^2 - c^2 t^2$ appearing in (B10) thereby yielding the special (side-constrained) error function $\Psi_c(\mathbf{f})$:

$$\Psi_c(\mathbf{f}) = \frac{1}{2} \sum_{i=1}^n [A_i x + B_i y + C_i z + D_i (ct) + E_i]^2, \quad (\text{B11})$$

where $A_i = 2(x_1 - x_i)$, $B_i = 2(y_1 - y_i)$, $C_i = 2(z_1 - z_i)$, $D_i = 2ct_i$, $E_i = r_i^2 - c^2 t_i^2 - r_1^2$. But (B11) can be rewritten as

$$\Psi_c(\mathbf{f}) = \frac{1}{2} (\mathbf{f}^T \mathbf{H} \mathbf{f} + \mathbf{v}^T \mathbf{f} + \alpha), \quad (\text{B12})$$

where the \mathbf{H} matrix is given by

$$\mathbf{H} = \begin{bmatrix} \sum_{i=1}^n A_i^2 & \sum_{i=1}^n A_i B_i & \sum_{i=1}^n A_i C_i & \sum_{i=1}^n A_i D_i \\ \sum_{i=1}^n A_i B_i & \sum_{i=1}^n B_i^2 & \sum_{i=1}^n B_i C_i & \sum_{i=1}^n B_i D_i \\ \sum_{i=1}^n A_i C_i & \sum_{i=1}^n B_i C_i & \sum_{i=1}^n C_i^2 & \sum_{i=1}^n C_i D_i \\ \sum_{i=1}^n A_i D_i & \sum_{i=1}^n B_i D_i & \sum_{i=1}^n C_i D_i & \sum_{i=1}^n D_i^2 \end{bmatrix}, \quad (\text{B13})$$

and the vector and scalar have the form

$$\begin{aligned} \mathbf{v}^T &= \left[2 \sum_{i=1}^n A_i E_i \quad 2 \sum_{i=1}^n B_i E_i \quad 2 \sum_{i=1}^n C_i E_i \quad 2 \sum_{i=1}^n D_i E_i \right], \\ \alpha &= \sum_{i=1}^n E_i^2. \end{aligned} \quad (\text{B14})$$

A comparison of (B1) with (B13) and (B14) indicates that

$$\mathbf{H} = 4\mathbf{K}^T \mathbf{K}, \quad \mathbf{v} = -8\mathbf{K}^T \mathbf{g}, \quad \alpha = 4\mathbf{g}^2. \quad (\text{B15})$$

Substituting (B15) into (B12) and recalling that $\mathbf{g} = \mathbf{K}\mathbf{f}$ gives

$$\begin{aligned} \Psi_c &= \frac{1}{2} [\mathbf{f}^T (4\mathbf{K}^T \mathbf{K}) \mathbf{f} - 8\mathbf{g}^T \mathbf{K} \mathbf{f} + 4\mathbf{g}^2] \\ &= 2\mathbf{g}^2 + 2\mathbf{f}^T \mathbf{K}^T \mathbf{K} \mathbf{f} - 4\mathbf{g}^T \mathbf{K} \mathbf{f} \\ &= \mathbf{g}^2 + (\mathbf{g}^2 + \mathbf{f}^T \mathbf{K}^T \mathbf{K} \mathbf{f} - 3\mathbf{g}^T \mathbf{K} \mathbf{f}) - \mathbf{g}^T \mathbf{K} \mathbf{f} \\ &\quad + \mathbf{f}^T \mathbf{K}^T \mathbf{K} \mathbf{f} \\ &= \mathbf{g}^2 + (\mathbf{g}^T \mathbf{g} + \mathbf{f}^T \mathbf{K}^T \mathbf{g} - 3\mathbf{g}^T \mathbf{g}) - \mathbf{g}^T \mathbf{K} \mathbf{f} \\ &\quad + \mathbf{f}^T \mathbf{K}^T \mathbf{K} \mathbf{f} \\ &= \mathbf{g}^2 + (\mathbf{f}^T \mathbf{K}^T \mathbf{g} + \mathbf{f}^T \mathbf{K}^T \mathbf{g} - 3\mathbf{f}^T \mathbf{K}^T \mathbf{g}) - \mathbf{g}^T \mathbf{K} \mathbf{f} \\ &\quad + \mathbf{f}^T \mathbf{K}^T \mathbf{K} \mathbf{f} \\ &= \mathbf{g}^T \mathbf{g} - \mathbf{f}^T \mathbf{K}^T \mathbf{g} - \mathbf{g}^T \mathbf{K} \mathbf{f} + \mathbf{f}^T \mathbf{K}^T \mathbf{K} \mathbf{f} \\ &= (\mathbf{g} - \mathbf{K} \mathbf{f})^T (\mathbf{g} - \mathbf{K} \mathbf{f}) = (\mathbf{g} - \mathbf{K} \mathbf{f})^2. \end{aligned} \quad (\text{B16})$$

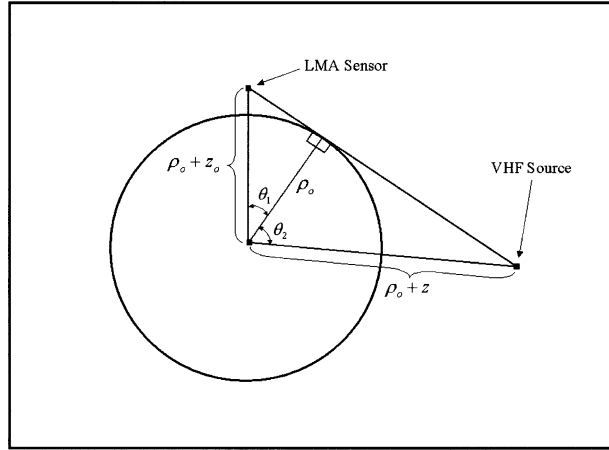


FIG. C1. Geometry for estimating horizontal range of LMA network. Atmospheric refraction and earth oblateness are neglected.

But this means that $\Psi_c(\mathbf{f})$ is of the form of (B2) with $\gamma = 0$. Hence, the minimum of $\Psi_c(\mathbf{f})$ is just the familiar least squares solution $\mathbf{f} = (\mathbf{K}^T \mathbf{K})^{-1} \mathbf{K} \mathbf{g}$. [This same result can be found by taking derivatives of (B11) with respect to x , y , z , and $f_4 = ct$, setting each to zero, and solving the resulting system of linear equations.]

Hence, the significance of the linear solution in (B1) is now clear. It is the minimum of an error function $\Psi(\mathbf{f})$ given in (B9) with the additional side constraint that $t_1 \equiv 0$. This linear solution should *not* be confused with the minimum of the closely related error function given in (B8). Since the difference in squared distances are used in (B9), an analytic solution was tractable. But the difference in regular distances used in (B8) has made it thus far too difficult to obtain an analytic solution (so a numerical method such as the Marquardt algorithm is applied). The importance of the linear solution in (B1) is that, though it is not exactly the minimum to the error function in (B8), it is a reasonably close initial guess; this fact makes it highly useful for obtaining solution convergence when Marquardt iterations are applied.

APPENDIX C

Maximum Ground-Range of the LMA Network

Neglecting atmospheric refraction and the oblateness of the earth, Fig. C1 shows one way to estimate the maximum range along the earth's surface between a LMA sensor at height z_o and a VHF source at altitude z . To obtain the maximum range for the LMA network,

TABLE C1. LMA maximum ground range. Numerical values of maximum ground range for VHF sources of various altitudes.

VHF source altitude, z (km)	Maximum ground range, Λ (km)
2	241.102
7	380.005
12	472.212
20	585.649

we select the highest antenna site in the network, which is at Putman, Alabama. The Putman antenna altitude is $z_o = 0.5211$ km, and the geodetic latitude of the site is $\phi_o = 34.8692474^\circ$. The spherical latitude of the site is then $\varphi_o = \tan^{-1}(b^2/a^2 \tan \phi_o) = 34.68895206^\circ$. We will assume a spherical earth with radius $\rho_o = \rho(\varphi_o) = (1/a^2 \cos^2 \varphi_o + 1/b^2 \sin^2 \varphi_o)^{-1/2} = 6371.187216$ km. Given the geometry in Fig. C1, the ground range Λ to the VHF source is

$$\Lambda = (\theta_1 + \theta_2) \rho_o$$

$$= \left[\cos^{-1} \left(\frac{\rho_o}{\rho_o + z_o} \right) + \cos^{-1} \left(\frac{\rho_o}{\rho_o + z} \right) \right] \rho_o. \quad (\text{C1})$$

In the main text of this writing, we considered VHF source altitudes of $z = 2$, 7 , and 12 km. We also anticipate that $z = 20$ km is a reasonable upper limit for most lightning VHF sources. Table C1 summarizes the ground ranges for the four source altitudes mentioned. Since most of our error plots in section 4 of the main text were performed for sources at $z = 7$ km, we chose a $7^\circ \times 7^\circ$ analysis region [i.e., one-half of this full range is $(3.5^\circ) (\pi/180) \rho_o = 389.194$ km, which just exceeds the value in Table C1 for $z = 7$ km].

REFERENCES

- Barnett, R. A., and M. R. Ziegler, 1989: *College Algebra*. 4th ed. McGraw-Hill Publishing Company, 517 pp.
- Bevington, P. R., 1969: *Data Reduction and Error Analysis for the Physical Sciences*. McGraw-Hill, 336 pp.
- Beyer, W. H., 1980: *Standard Mathematical Tables*. 25th ed. CRC Press, 613 pp.
- DMA, 1991: Department of defense world geodetic system 1984. 2d ed. Defense Mapping Agency Tech. Rep. 8350.2, 12 pp.
- Koshak, W., and R. Solakiewicz, 1996: On the retrieval of lightning radio sources from time-of-arrival data. *J. Geophys. Res.*, **101**, 26 631–26 639.
- Marquardt, D. W., 1963: An algorithm for least-squares estimation of nonlinear parameters. *J. Soc. Ind. Space Appl. Math.*, **11**, 431–441.
- Twomey, S. A., 1977: *Introduction to the Mathematics of Inversion in Remote Sensing and Indirect Measurements*. Dover Publications, 243 pp.